NANO LETTERS

pubs.acs.org/NanoLett Letter

Interplay between Local Moment and Itinerant Magnetism in the Layered Metallic Antiferromagnet $TaFe_{1.14}Te_3$

Sae Young Han, Evan J. Telford,* Asish K. Kundu, Sylvia J. Bintrim, Simon Turkel, Ren A. Wiscons, Amirali Zangiabadi, Eun-Sang Choi, Tai-De Li, Michael L. Steigerwald, Timothy C. Berkelbach, Abhay N. Pasupathy, Cory R. Dean, Colin Nuckolls, and Xavier Roy*

Cite This: *Nano Lett.* 2023, 23, 10449−10457 Read Online

ACCESS | Metrics & More | Article Recommendations | Supporting Information

ABSTRACT: Two-dimensional antiferromagnets have garnered considerable interest for the next generation of functional spintronics. However, many bulk materials from which two-dimensional antiferromagnets are isolated are limited by their air sensitivity, low ordering temperatures, and insulating transport properties. $TaFe_{1+y}Te_3$ aims to address these challenges with increased air stability, metallic transport, and robust antiferromagnetism. Here, we synthesize $TaFe_{1+y}Te_3$ (y = 0.14), identify its structural, magnetic, and electronic properties, and elucidate the relationships between them. Axial-dependent high-field magnetization measurements on $TaFe_{1.14}Te_3$ reveal saturation magnetic fields ranging between 27 and 30 T with saturation magnetic moments of 2.05−2.12 μ_B. Magnetotransport measurements confirm that $TaFe_{1.14}Te_3$ is metallic with strong coupling between magnetic order and electronic transport. Angle-resolved photoemission spectroscopy measurements across the magnetic transition uncover a complex interplay between itinerant electrons and local magnetic moments that drives the magnetic transition. We demonstrate the ability to isolate few-layer sheets of $TaFe_{1.14}Te_3$, establishing $TaFe_{1.14}Te_3$ as a potential platform for two-dimensional spintronics.

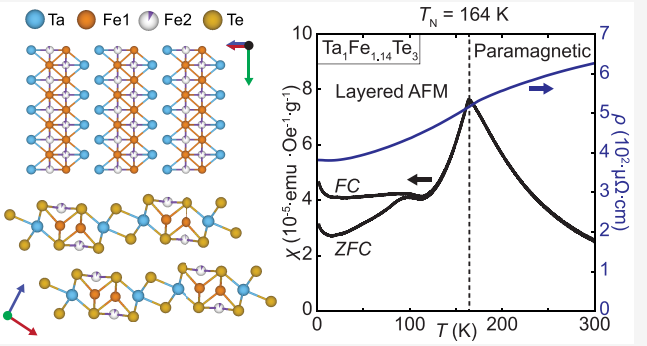

KEYWORDS: *van der Waals materials, magnetic metals, layered antiferromagnetism, magnetotransport, high-field magnetic susceptibility, angle-resolved photoemission spectroscopy*

Identifying candidate low-dimensional materials combining metallic transport behavior with robust antiferromagnetic order is crucial to advancing spin-based nanotechnologies. van der Waals (vdW) magnets, in particular, provide an ideal platform for fabricating atomically thin spintronics and magneto-optic devices,[1−5] as they possess diverse magnetic phases and electronic properties that persist down to the two-dimensional (2D) limit. Within this family of materials, those exhibiting metallic electronic transport have received intense attention due to their potential functionality as spin injectors,[6,7] magnetic tunnel junction electrodes,[8] or spin−orbit torque devices.[9,10] Among the available 2D magnets, layered antiferromagnets are exceptionally attractive due to the increased resilience to external magnetic fields,[11,12] sensitivity of electrical resistance to field-induced antiferromagnetic-to-ferromagnetic transitions,[13,14] faster spin dynamics,[15] utility in high-frequency spin−orbit torque experiments,[16] and capability for higher packing density than ferromagnets in memory storage devices due to the absence of stray fields.[17] Despite an obvious need, vdW materials integrating metallic behavior with layered antiferromagnetic order are notably scarce.[18] $TaFe_{1+y}Te_3$[19−22] is one candidate to overcome many existing limitations of vdW magnets, boasting a high Néel temperature ranging between 160 and 200 K,[19,21,23−25] metallic charge transport properties,[19,23,24,26,27] and stability under ambient conditions, showcasing its promise for metallic antiferromagnet-based spintronics.

In this work, we synthesize $TaFe_{1+y}Te_3$ (y = 0.14) and explore its electronic and magnetic properties, uncovering its potential for atomic-scale spintronic devices based on vdW materials. Temperature- and magnetic-field-dependent magnetization measurements reveal a paramagnetic-to-antiferromagnetic transition at 164 K followed by a transition into a spin-glassy magnetic phase below ∼100 K. At liquid helium temperature, full magnetization saturation occurs only at 27−30 T for all morphological directions, with a saturation

Received: August 17, 2023
Revised: October 28, 2023
Accepted: October 31, 2023
Published: November 7, 2023

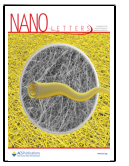

https://doi.org/10.1021/acs.nanolett.3c03112
Nano Lett. 2023, 23, 10449−10457

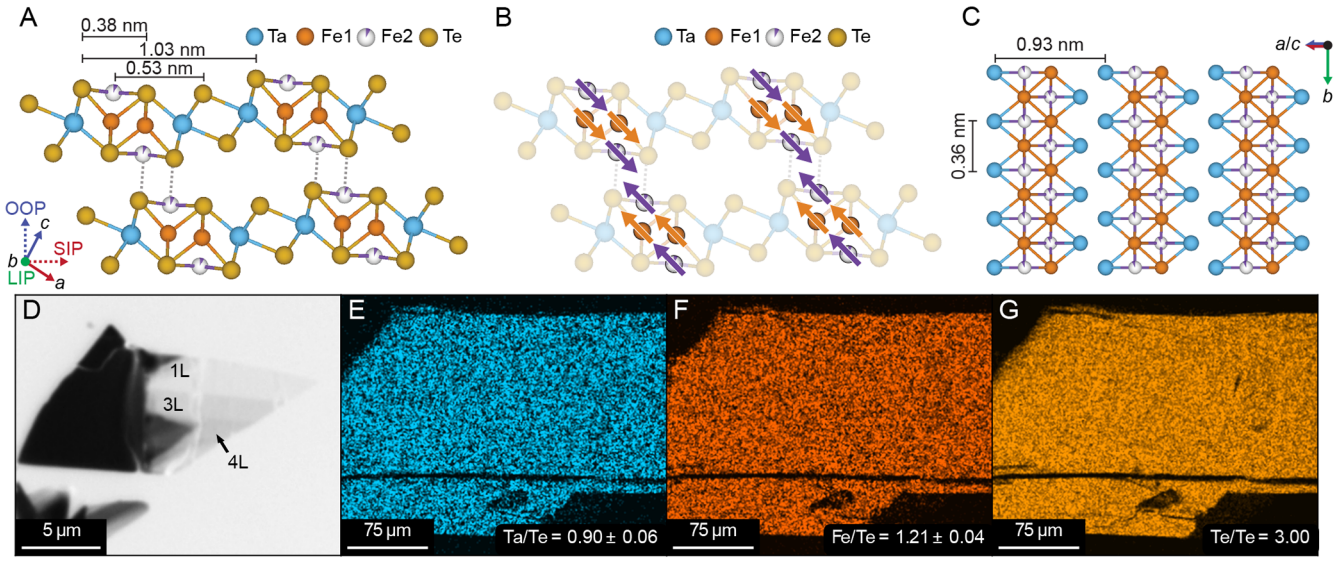

Figure 1. Structure and composition of $TaFe_{1.14}Te_3$. (A) Crystal structure of $TaFe_{1.14}Te_3$ viewed along the crystallographic *b*-axis. Morphological long in-plane (LIP) (green), short in-plane (SIP) (red), and out-of-plane (OOP) (blue) directions are shown relative to the crystallographic *a*-, *b*-, and *c*-axes. (B) Crystal structure of $TaFe_{1.14}Te_3$ viewed along the crystallographic *b*-axis with the orientation of the Fe1 (orange arrows) and Fe2 (purple arrows) magnetic moments in the antiferromagnetic state overlaid. (C) Crystal structure of $TaFe_{1.14}Te_3$ viewed along a direction that clearly displays the Fe1/Fe2 chain structure. The Te atoms are removed for clarity. (D) False-colored optical microscope image of a $TaFe_{1.14}Te_3$ flake exfoliated onto polydimethylsiloxane (PDMS). The corresponding layer numbers for different regions were determined by atomic force microscopy and optical contrast (Figure s1). (E–G) Ta (E), Fe (F), and Te (G) elemental maps of a single crystal of $TaFe_{1.14}Te_3$ as determined by SEM/EDX. The bottom right inset of each elemental map gives the corresponding elemental composition normalized to Te. In (E) and (F), the error bars represent the standard deviation of multiple measurements between various crystals and growth batches.

magnetization moment of 2.05–2.12 μ_B. Through density functional theory (DFT) calculations, we confirm the stability of the metallic antiferromagnetic phase and characterize its electronic structure. Longitudinal magnetotransport and Hall measurements verify the metallic nature and demonstrate a strong coupling between magnetic order and electronic transport. Angle-resolved photoemission spectroscopy (ARPES) measurements further support the metallic nature of $TaFe_{1.14}Te_3$ and reveal a complex interplay between local moment and itinerant magnetism. We also demonstrate the ability to isolate few-layer flakes of $TaFe_{1.14}Te_3$ through mechanical exfoliation, solidifying its practicality for spintronic applications.

Single crystals of $TaFe_{1.14}Te_3$ are grown using the chemical vapor transport method (see the methods for full details). Tantalum, iron, tellurium, and $TeCl_4$ powders are pressed into a pellet and sealed in a fused silica tube under vacuum. After 7 days in a temperature gradient of 700 to 600 °C, needle-like crystals are obtained in the sink side of the tube. An Fe2 concentration of 0.14 was not explicitly chosen, but simply a result of our optimized growth process. We note that attempts at systematically varying Fe2 stoichiometry were unsuccessful. We performed single crystal X-ray diffraction (SCXRD) to determine the structure (Figure 1A–C). The low-dimensional layered telluride $TaFe_{1.14}Te_3$ crystallizes in the $P2_1/m$ space group. The structure features Ta–Fe1–Fe1–Ta ribbons aligned along the *b*-axis while sandwiched between Te layers. Along the ribbon, the Ta atoms are octahedrally coordinated by six Te atoms, and the Fe1 atoms, which make a one-dimensional zigzag chain, are tetrahedrally coordinated by four Te atoms. Unlike the Fe1 site, the Fe2 site is partially occupied, and the Fe2 atom nestles in the center of the square pyramid formed by Te atoms (Figure 1A). Single crystals are stable under ambient conditions, and the layered nature of the structure, along with the corresponding interlayer vdW bonds, allows for the isolation of air-stable few-layer flakes of $TaFe_{1.14}Te_3$ through mechanical exfoliation down to the monolayer limit (Figure 1D). Corresponding tapping-mode atomic force microscopy images of an exfoliated sample can be found in Figure s1. Previously reported neutron diffraction measurements on $TaFe_{1+y}Te_3$ determined that the magnetic moments are localized on the Fe atoms. The magnetic structure is identified as A-type antiferromagnetic with Fe1 spins coupling ferromagnetically within the layers and antiferromagnetically between the layers.[23] The Fe2 spins within each layer align parallel to the Fe1 spins (Figure 1B). The atomic ratio of different constituent elements was determined through SCXRD occupancy refinement (Table s1) and confirmed by energy dispersive X-ray spectroscopy (EDX) on freshly cleaved samples (Table s2). Corresponding scanning electron microscopy (SEM)/EDX elemental maps of a $TaFe_{1.14}Te_3$ single crystal were obtained for Ta, Fe, and Te, with each collection normalized to Te. All elemental maps display a homogeneous distribution, demonstrating that there is no evidence of Fe clustering down to the micrometer scale (Figure 1E–G).

Since the Fe2 site is only partially occupied, we first characterize the uniformity of the Fe2 distribution and the impact of Fe2 on the local electronic properties. We performed scanning tunneling microscopy (STM) and spectroscopy (STS) on cleaved bulk $TaFe_{1.14}Te_3$. In Figure 2A, we present an atomically resolved STM image of the vdW plane at 7.5 K. The selected distances, determined by a fast Fourier transform (FFT) of the real-space STM topography, are as follows: Te···Te (nearest neighbor) = 0.35, 0.36 nm, Fe2···Te = 0.52 nm, and Te···Te (next nearest neighbor) = 1.01 nm (Figure 2B).

https://doi.org/10.1021/acs.nanolett.3c03112
Nano Lett. 2023, 23, 10449–10457

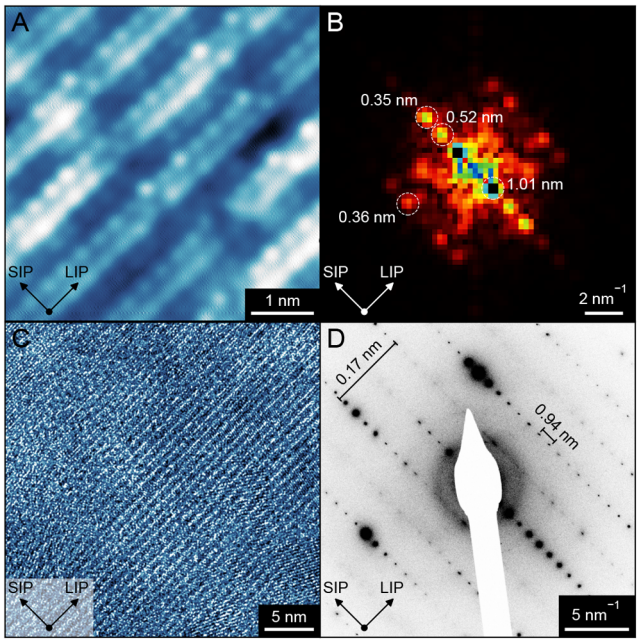

Figure 2. Atomic-scale characterization of $TaFe_{1.14}Te_3$. (A) STM image of $TaFe_{1.14}Te_3$ cleaved along the vdW gap. The image was obtained at T = 7.5 K in constant current mode (V_b = 400 mV, I = 50 pA). (B) Corresponding FFT of the STM image. Select periodicities are denoted by dashed white circles. (C) TEM micrograph of an exfoliated $TaFe_{1.14}Te_3$ flake with a thickness <50 nm viewed along the OOP direction. (D) Corresponding electron diffraction image of the same flake in (C). Select *d*-spacings are denoted by solid black bars. In all panels, the orientation of the images with respect to the morphological SIP and LIP directions is given in the bottom left inset.

These values are in good agreement with those obtained from SCXRD (Figure 1A). With its atomic precision, STM allows us to view the topographical corrugation of the Fe chains in detail. We observe inhomogeneity of intensity in the image, which may indicate random nanometer-scale clustering of Fe2 in the crystal, as previously hypothesized in a Mössbauer spectroscopy study of $TaFe_{1+y}Te_3$.[20] This clustering may be responsible for the spin-glass phase that emerges below 100 K (see the discussion below). Corresponding STS measurements show a metallic-like density of states (DOS) at all points across multiple Fe chains, revealing that the occupancy of the Fe2 site does not significantly impact the local electronic structure (Figure s2).

To confirm that the quasi-one-dimensional nature of the structure persists in exfoliated flakes, we performed transmission electron microscopy (TEM) and corresponding selected-area electron diffraction (SAED) measurements on an exfoliated flake of $TaFe_{1.14}Te_3$ with a thickness <50 nm (Figure 2C, D; see the methods for details). The diffraction pattern shows that the crystallinity is intact in the exfoliated flake of $TaFe_{1.14}Te_3$. This is also seen in the real-space image, in which we observe distinct lines of atoms along the direction of the chains, as depicted in Figure 1C. Select atomic distances from the SAED image are 0.17 nm for the close-range Fe atoms and 0.94 nm for the interchain Fe atoms (Figure 2D), in good agreement with those obtained from SCXRD (Table s1 and Figure 1A, C) and STM (Figure 2A, B).

We measured the magnetic susceptibility (χ) of $TaFe_{1.14}Te_3$ as a function of the applied magnetic field (H) and temperature (T). In Figure 3A, we present χ vs T curves with H along the SIP, LIP, and OOP morphological directions (see Figure 1A for reference to crystallographic axes). When cooling the sample from room temperature, the measurements show a paramagnetic-to-antiferromagnetic phase transition, characterized by a peak in χ at the Néel temperature T_N = 164 ± 2 K (Figures s3, s4 for additional data). The Néel temperature is also confirmed through H-dependent heat capacity measurements (Figure s5). Below the Néel temperature, the zero-field-cooled (ZFC) and field-cooled (FC) branches separate, signaling the emergence of a spin-glassy phase below ∼100 K (Figures s6−s9 for a more detailed analysis).[25] This behavior, often associated with competing antiferromagnetic and ferromagnetic interactions, has been observed in other $TaFe_{1+y}Te_3$ stoichiometries[25] and certain $Fe_xMn_{1-x}TiO_3$ systems where long-range antiferromagnetic and reentrant spin-glass phases can coexist.[28−31] The extracted Weiss temperatures (Θ_w) in the paramagnetic phase convey strong ferromagnetic coupling, with values of 154, 158, and 149 K for the OOP, LIP, and SIP directions, respectively (inset of Figure 3A). The Curie−Weiss fit estimates an effective magnetic moment (μ_{eff}) ranging between 4.26 and 4.28 μ_B for all morphological directions, in line with the expected local moment of 4 μ_B for a majority high-spin tetrahedral Fe^{2+} ion (Figure s23).[32]

Figure 3B−D plots the magnetization (M) vs applied H along all morphological directions (see Figure 1A) up to 35 T at various T. The OOP- and SIP-oriented M vs H curves at 1.5 K reveal a series of steps in M between 9 and 15 T after which M continues to increase until saturating at 29 and 30 T, respectively (Figure 3B, 3D, and Figure s10). The exact nature of these steps is unclear without further measurements of the high-field magnetic structure but are likely due to metamagnetic transitions (see Figures s11 and s12 for additional data). The LIP-oriented M vs H curve at 1.5 K is linear up to 27 T after which it saturates, indicating a gradual spin canting process (Figure 3C). This confirms the LIP direction as the hard axis (Figure 3C and Figure s10). At 1.5 K, the sample reaches a saturation magnetic moment for all axial orientations ranging between 2.05 and 2.12 μ_B, which is significantly smaller than the μ_{eff} determined for the high-T paramagnetic phase. As expected, increasing T decreases the saturation magnetic moment and the H value at which the moment saturates.

Our measured saturation moments of ∼2 μ_B are consistent with those assigned previously based on neutron diffraction measurements of the antiferromagnetic phase.[23] The discrepancy between μ_{eff} and the measured saturation magnetic moment implies that both local moment and itinerant magnetism coexist in $TaFe_{1.14}Te_3$. For further insight, we performed first-principles DFT calculations on $TaFe_{1+y}Te_3$ with y = 0, 0.25, and 1 with various magnetic orderings (see the methods for details). We find that the antiferromagnetic order shown in Figure 1B, with intraplane ferromagnetic order and interplane antiferromagnetic order, is always electronically stable and typically lower in energy than other magnetic orderings (including nonmagnetic), although the energy differences are oftentimes small. Löwdin charge analysis of Fe atoms gives a positive charge of 0.3−0.5 and a magnetic moment of 2.2−2.4 μ_B, for both Fe1 and Fe2 (Table s3), in good agreement with our measured saturation moment. Because DFT with common functionals is not appropriate for strongly correlated electrons, the agreement with experiment supports the picture that electron itinerancy is responsible for the suppression of the magnetic moment.

https://doi.org/10.1021/acs.nanolett.3c03112
Nano Lett. 2023, 23, 10449−10457

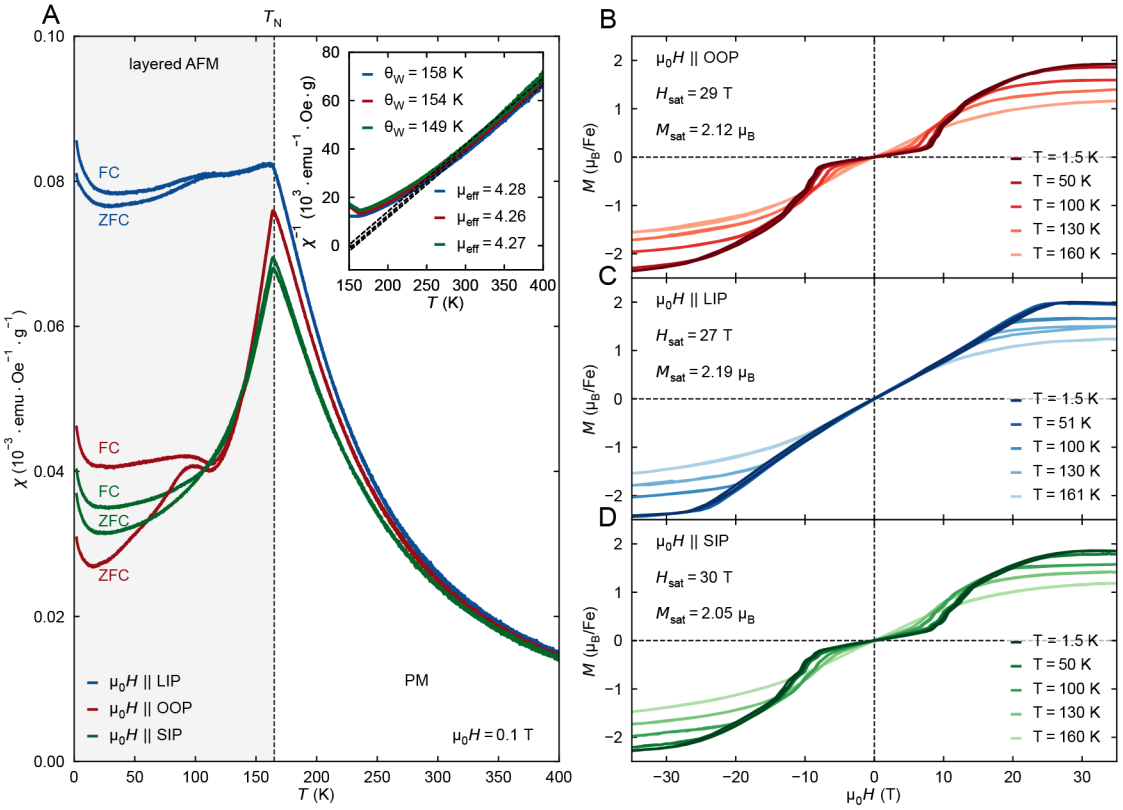

Figure 3. High-field magnetic properties of $TaFe_{1.14}Te_3$. (A) χ versus T for H oriented along the SIP (solid green lines), LIP (solid blue lines), and OOP (solid red lines) directions. Both zero-field-cooled (ZFC) and field-cooled (FC) traces are shown. All traces were collected with a field of H = 0.1 T. The extracted Néel temperature is shown by a black dashed line. Layered antiferromagnetic and paramagnetic phases are denoted by gray and white regions, respectively. The inset shows inverse χ versus T for H oriented along the SIP (solid green line), LIP (solid blue line), and OOP (solid red line) directions. Dashed black lines are linear fits of each trace. The extracted Θ_w and μ_{eff} are given in the upper left and lower right insets, respectively. (B–D) M versus H at different Ts for H oriented along the OOP (B), LIP (C), and SIP (D) directions. In each plot, the extracted saturation magnetization (M_{sat}) and H_{sat} are given in the inset. Note that because both the OOP and SIP directions contain a component parallel to the Fe1/Fe2 spin directions, they both exhibit metamagnetic transitions. The LIP direction, however, is completely perpendicular to the Fe1/Fe2 spin directions and only displays a gradual spin-canting process.

Although the character of the bands near the Fermi energy (E_F) is found to be a complex and nearly equal mixture of Fe 3d, Ta 5d and Te 5p orbitals (Figures s20–s21), all DFT calculations predict a metallic electronic structure, whose properties we study further by magnetotransport measurements.

In Figure 4, we report the magnetotransport of $TaFe_{1.14}Te_3$ single crystals. Transport devices were fabricated using a microsoldering technique which consists of drawing micron-scale contacts with Field's metal using a micromanipulator (see the methods for details).[33,34] Figure 4A plots the zero-field resistivity (ρ) of $TaFe_{1.14}Te_3$ versus T. Overall metallic behavior is observed with ρ decreasing with decreasing T. At T = 175 ± 3 K, there is a sharp jump in the derivative of ρ versus T, which is attributed to the onset of antiferromagnetic order. Below this temperature, ρ varies approximately as T^2, saturating to a constant value at low T.

Figure 4D presents the H dependence of the magnetoresistance ratio (MRR). MRR is defined as $MRR = [(R(H) - R(H = 0))/R(H = 0)] \times 100$, where H is oriented along the OOP direction. Above T_N, the system is in the paramagnetic phase characterized by a broad negative MRR (nMRR) due to the field-induced suppression of spin-flip scattering between conduction electrons and local magnetic moments. Well below T_N at 1.5 K, we observe a negligible MRR up to a critical field of H_C = 8.5 ± 0.2 T above which the absolute value of MRR sharply increases and continues to increase linearly for $H > H_C$. The response of MRR closely follows the measured M vs H traces (Figure 4B and Figures s13–s17), indicating that H_C is correlated with the jump in M vs H. As T increases, H_C decreases toward zero at T_N, consistent with the magnetization measurements. These results demonstrate that $TaFe_{1.14}Te_3$ exhibits a relatively strong coupling between its electrical properties and magnetic order. The fact that MRR decreases as M increases suggests the primary mechanism could be a field-induced suppression of interlayer spin-flip scattering; however, elucidating the exact mechanism behind this coupling will require further measurements of the field-induced magnetic structure.

The coupling between the electrical and magnetic properties can also be seen in the Hall measurements presented in Figure 4C. In magnetic materials, the Hall resistance (R_{Hall}) is typically determined by two components arising from the external and internal magnetic fields.[35] In general, R_{Hall} is proportional to the applied H (the slope of which is related to the carrier density) plus sample magnetization. These two contributions can be clearly seen in Hall measurements across the magnetic transition (Figure 4C; see also Figures s13–s18).

https://doi.org/10.1021/acs.nanolett.3c03112
Nano Lett. 2023, 23, 10449–10457

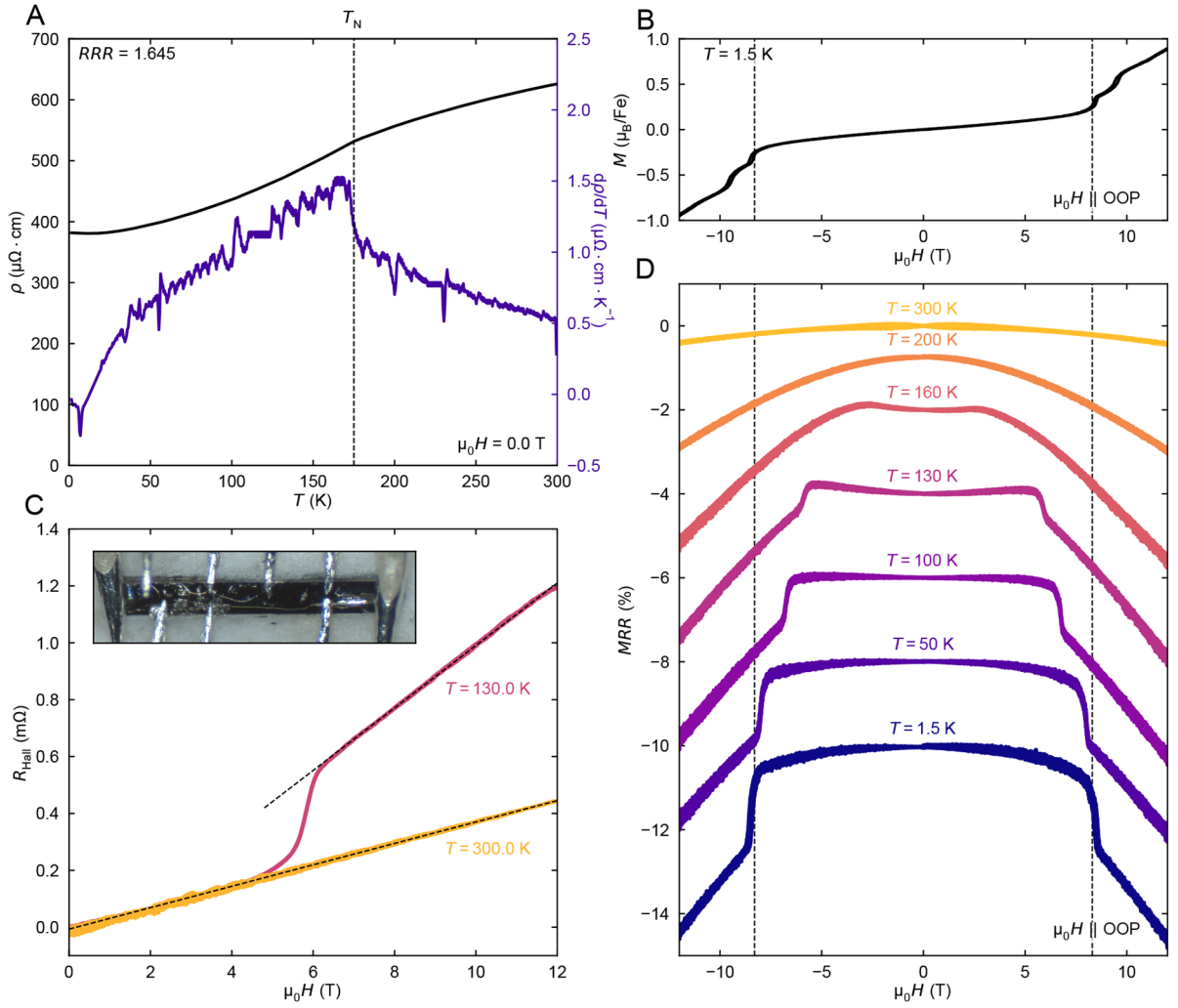

Figure 4. Electronic transport properties of $TaFe_{1.14}Te_3$. (A) ρ (left) and derivative of ρ (right) versus T at zero H. The extracted residual resistivity ratio ($RRR = R(300\ K)/R(2K)$) is given in the inset. The extracted T_N is shown by a black dashed line. (B) M versus H at 1.5 K for H parallel to the OOP direction. (C) R_{Hall} versus H above (solid yellow line) and below (solid magenta line) T_N. Two distinct linear regions (denoted by dashed black lines) are observed below T_N, whereas a single linear region is observed above T_N. Additional traces at different temperatures can be found in Figure s18. An optical image of the device is shown in the inset. (D) Magnetoresistance ratio, $MRR = [(R(H)-R(H=0))/R(H=0)] \times 100$, versus H at various T for fields parallel to the OOP direction. Both forward and backward H sweeps are shown and the curves are offset for clarity. The T values at which each trace was taken are given in the inset. The dashed black line indicates the critical field of the first metamagnetic transition observed at 1.5 K.

Above T_N (at 300 K), since the sample has negligible magnetization (Figure s15), the R_{Hall} versus H is linear, from which we extract a corresponding carrier density of $(1.30 \pm 0.03) \times 10^{21}$ cm^{-3}, consistent with previous measurements on similar $TaFe_{1+y}Te_3$ stoichiometries.[24,26] Below T_N (130 K), R_{Hall} versus H is linear at low H with the same slope as the 300 K trace, corresponding to the normal Hall contribution from external H. Once H reaches H_C, R_{Hall} sharply increases and then continues to increase linearly with H for $H > H_C$. The slope of R_{Hall} versus H when $H > H_C$ is larger than the slope for $H < H_C$ due to the additional Hall component from the linear sample magnetization (Figure s14). The slope of R_{Hall} versus H for both $H > H_C$ and $H < H_C$ has a nonmonotonic temperature dependence which may arise from temperature-dependent magnetic fluctuations (Figure s18).[24] Other factors, such as temperature- and field-dependent changes in the band structure, could contribute to R_{Hall}. However, our results bear similarities to other $TaFe_{1+y}Te_3$ stoichiometries[24,26] and ARPES measurements on $TaFe_{1.14}Te_3$ (see below) show only minor changes in the band structure across the magnetic transition, indicating R_{Hall} is primarily determined by the sample carrier density and the sample magnetization (see Figures s13–s18 for additional data). This clear effect of sample magnetization on the measured R_{Hall} further demonstrates the strong coupling between magnetism and electronic properties in $TaFe_{1.14}Te_3$.

To experimentally probe the electronic structure of $TaFe_{1.14}Te_3$, we performed ARPES on a freshly cleaved surface (vdW plane) under ultrahigh vacuum (UHV) across the magnetic transition (Figure 5). The Fermi surfaces at 20 and 210 K are shown in Figure 5A, B, respectively. Two sets of periodic wave-like Fermi surfaces (FSs) are identified, indicated by α and α' in Figure 5A. The modulated FSs perpendicular to Fe1−Te chain directions (i.e., $\bar{\Gamma}$–$\bar{Y}$) points to

https://doi.org/10.1021/acs.nanolett.3c03112
Nano Lett. 2023, 23, 10449−10457

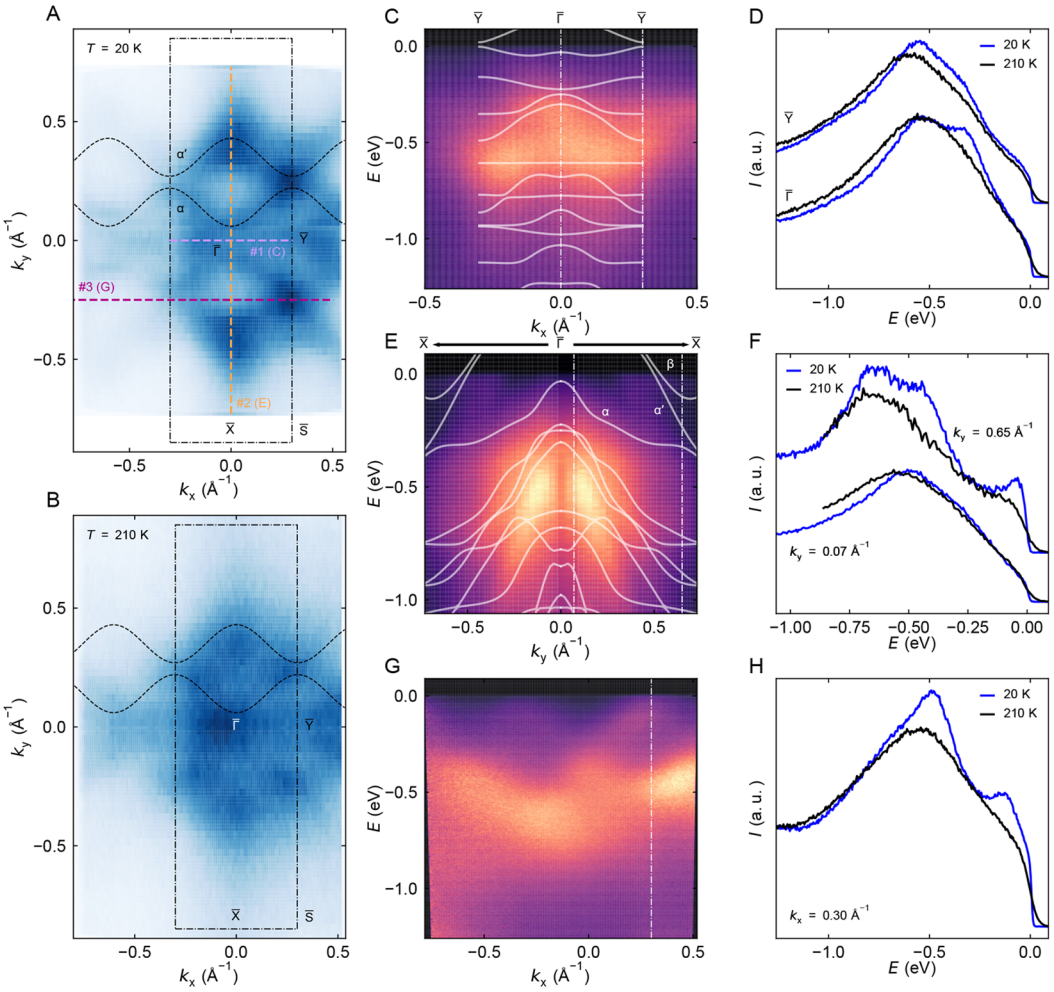

Figure 5. Evolution of the Fermi surface and electronic states of $TaFe_{1.14}Te_3$ across the magnetic transition. ARPES Fermi surface maps at 20 K (A) and 210 K (B). Dark blue (white) colors correspond to high (low) photoelectron intensity. The Fermi surfaces are symmetrized at k_y = 0 Å^{-1}. In both (A) and (B), the black dashed rectangle represents the surface Brillouin zone. The $\bar{\Gamma}$–$\bar{X}$ and $\bar{\Gamma}$–$\bar{Y}$ directions are along the (LIP) and perpendicular (SIP) Fe–Te chains, respectively. (C) ARPES intensity map along the $\bar{Y}$–$\bar{\Gamma}$–$\bar{Y}$ direction is shown as cut #1 (purple dashed line in (A)). Calculated nonmagnetic band structure is overlaid as semi-transparent white lines. (D) Energy distribution curves (EDCs) at $\bar{\Gamma}$ and $\bar{Y}$ symmetry points (vertical dashed white lines in (C)) at 20 K (solid blue lines) and 210 K (solid black lines). (E) ARPES intensity map along the $\bar{X}$–$\bar{\Gamma}$–$\bar{X}$ direction is shown as cut #2 (orange dashed line in (A)). Calculated nonmagnetic band structure is overlaid as semitransparent white lines. (F) EDCs at k_y = 0.07 Å^{-1} (α) and k_y = 0.65 Å^{-1} (β) (vertical dashed white lines in (E)) at 20 K (solid blue lines) and 210 K (solid black lines). (G) ARPES intensity map along cut #3 (magenta dashed lined in (A)). (H) EDCs at k_x = 0.30 Å^{-1} (vertical dashed white line in (G)) at 20 and 210 K. All data were acquired with a photon energy of 21.22 eV. For (C), (E), and (G), purple (yellow) colors correspond to low (high) photoelectron intensity. All calculated band structures were scaled down by 1.4 and shifted down by 0.2 eV.

significant interchain interactions. The FS features look similar between the paramagnetic and antiferromagnetic phases, except for the thermal broadening, consistent with the previous report.[27] The broadened spectroscopic features are likely a result of the disorder associated with the Fe2 site.

The ARPES intensity maps along the $\bar{Y}$–$\bar{\Gamma}$–$\bar{Y}$ and $\bar{X}$–$\bar{\Gamma}$–$\bar{X}$ paths in the low-T antiferromagnetic phase are shown in Figure 5C, 5E (cut #1 and #2 in Figure 5A). ARPES intensity maps are compared to our DFT band structures of nonmagnetic $TaFeTe_3$, where the E_F was empirically shifted to best match the ARPES data (additional orbital-resolved band structures and partial density of states can be found in Figures s20–s21). Along the $\bar{X}$–$\bar{\Gamma}$–$\bar{X}$ path, we observe two hole-like bands, α and α', crossing E_F. Another less dispersive band (β) is also observed near E_F. Overall, experimental ARPES intensity maps show reasonable agreement with our DFT calculations, when the bandwidth of the latter is reduced by a factor of 1.4 (Figure 5C, 5E). While the disorder broadens the ARPES data and makes a detailed comparison with DFT challenging, the best agreement is achieved when we renormalize the DFT bands. This suggests the importance of strong electron correlations that are absent in standard DFT. However, to precisely determine the correlation effect, additional high-resolution ARPES studies and dynamical mean-field theory (DMFT) calculations are required. Figure 5D displays the energy distribution curves (EDCs) at $\bar{\Gamma}$ and $\bar{Y}$ points across the magnetic transition. We observe a distinct change in spectral intensity and a transfer of spectral weight from high-to-low binding energy along with a slight shift in the energy of the bands. A more detailed T dependence reveals that the most significant changes occur below ~100 K (Figure s22). The evolution of EDCs across the magnetic transition for the α and β bands is shown in Figure 5F. Below the magnetic transition, the β band shows an enhancement in the

https://doi.org/10.1021/acs.nanolett.3c03112
Nano Lett. 2023, 23, 10449–10457

quasiparticle (QP) spectral weight near E_F. However, no such change was observed for the α band. ARPES intensity maps along cut #3 (shown as a dashed line in Figure 5A) and EDCs are shown in Figure 5G, 5H, respectively. A strong enhancement of the integrated spectral weight of ∼16% is observed within 0 to −1.25 eV in the antiferromagnetic phase relative to the paramagnetic phase. These combined results reflect that the magnetic transition is driven by electronic structure reconstruction rather than Fermi surface nesting.

Our results suggest that the electronic states undergo a band-dependent reconstruction across the magnetic transition due to the interplay between orbital and spin degrees of freedom. This behavior is known to occur in other systems containing local moments and itinerant electrons,[36−39] such as heavy Fermion compounds,[40] Fe-based superconductors,[41,42] and other strongly correlated transition-metal oxides.[43,44] The coexistence of itinerant and local-moment magnetism in $TaFe_{1.14}Te_3$, combined with the fact that $TaFe_{1.14}Te_3$ can be exfoliated down to atomically thin flakes, providing new opportunities to study such correlated magnetic systems in the 2D limit.

Through a combination of magnetic, electronic, and transport measurements, supported by first-principles DFT calculations, we resolve the interplay between the magnetic and electronic properties in the layered vdW magnet $TaFe_{1.14}Te_3$. We performed high-field magnetometry, revealing the full direction-dependent magnetic properties. Calculations and magnetotransport measurements confirm the metallic nature of $TaFe_{1.14}Te_3$ and display strong coupling between electronic transport properties and magnetic order. Temperature-dependent ARPES measurements show minor band shifts and strong spectral weight renormalization across the magnetic transition. This, combined with a low observed saturation moment of 2.05−2.12 μ_B found in both the high-field magnetometry measurements and DFT calculations, indicates a complex interplay between local moment and itinerant magnetism in $TaFe_{1.14}Te_3$. Finally, we demonstrate the isolation of air-stable few-layer flakes of $TaFe_{1.14}Te_3$ down to the monolayer limit. Altogether, our results establish $TaFe_{1.14}Te_3$ as an exciting material for 2D spintronics, manifesting robust A-type antiferromagnetism, metallic transport properties, and stability under ambient conditions. Furthermore, the intersection of local-moment and itinerant magnetism typically occurs in correlated electronic systems, offering $TaFe_{1.14}Te_3$ as a promising platform for studying magnetism in 2D correlated electronic materials.

■ ASSOCIATED CONTENT

Supporting Information

(PDF). The Supporting Information is available free of charge at https://pubs.acs.org/doi/10.1021/acs.nanolett.3c03112.

Additional experimental details and methods are outlined. Characterization of exfoliated flakes of $TaFe_{1.14}Te_3$, STM measurements of $TaFe_{1.14}Te_3$ single crystals, extended magnetic measurements of $TaFe_{1.14}Te_3$ single crystals, magnetic-field-dependent heat capacity measurements of $TaFe_{1.14}Te_3$ single crystals, detailed characterization of the spin glass phase, additional high field magnetic measurements on $TaFe_{1.14}Te_3$ single crystals, detailed analysis of magnetic and transport measurements, calculated band structures for $TaFe_1Te_3$ and $TaFe_2Te_3$, calculated PDOS for $TaFe_1Te_3$ and $TaFe_2Te_3$, temperature-dependent ARPES data, oxidation state characterization of $TaFe_{1.14}Te_3$ single crystals, table of additional details of SCXRD, statistical analysis on the elemental composition of $TaFe_{1.14}Te_3$ single crystals, and theoretical charge and magnetic moment of $TaFe_1Te_3$, $TaFe_{1.25}Te_3$, and $TaFe_2Te_3$ (PDF)

■ AUTHOR INFORMATION

Corresponding Authors

Evan J. Telford − *Department of Chemistry, Columbia University, New York, New York 10027, United States; Department of Physics, Columbia University, New York, New York 10027, United States;* orcid.org/0000-0002-9494-9166; Email: ejt2133@columbia.edu

Xavier Roy − *Department of Chemistry, Columbia University, New York, New York 10027, United States;* orcid.org/0000-0002-8850-0725; Email: xr2114@columbia.edu

Authors

Sae Young Han − *Department of Chemistry, Columbia University, New York, New York 10027, United States*

Asish K. Kundu − *Condensed Matter Physics and Materials Science Department, Brookhaven National Laboratory, Upton, New York 11973, United States;* orcid.org/0000-0003-2199-1053

Sylvia J. Bintrim − *Department of Chemistry, Columbia University, New York, New York 10027, United States*

Simon Turkel − *Department of Physics, Columbia University, New York, New York 10027, United States*

Ren A. Wiscons − *Department of Chemistry, Columbia University, New York, New York 10027, United States;* Present Address: Department of Chemistry, Amherst College, Amherst, MA, 01002, United States

Amirali Zangiabadi − *Department of Applied Physics and Applied Mathematics, Columbia University, New York, New York 10027, United States*

Eun-Sang Choi − *National High Magnetic Field Laboratory, Tallahassee, Florida 32310, United States*

Tai-De Li − *Nanoscience Initiative at Advanced Science Research Center, Graduate Center of the City University of New York, New York, New York 10031, United States; Department of Physics, The City College of New York, New York, New York 10031, United States*

Michael L. Steigerwald − *Department of Chemistry, Columbia University, New York, New York 10027, United States*

Timothy C. Berkelbach − *Department of Chemistry, Columbia University, New York, New York 10027, United States;* orcid.org/0000-0002-7445-2136

Abhay N. Pasupathy − *Department of Physics, Columbia University, New York, New York 10027, United States; Condensed Matter Physics and Materials Science Department, Brookhaven National Laboratory, Upton, New York 11973, United States;* orcid.org/0000-0002-2744-0634

Cory R. Dean − *Department of Physics, Columbia University, New York, New York 10027, United States*

Colin Nuckolls − *Department of Chemistry, Columbia University, New York, New York 10027, United States;* orcid.org/0000-0002-0384-5493

Complete contact information is available at:

https://doi.org/10.1021/acs.nanolett.3c03112
Nano Lett. 2023, 23, 10449−10457

https://pubs.acs.org/10.1021/acs.nanolett.3c03112

Author Contributions

S.Y.H. and E.J.T. collected and analyzed the SCXRD data. S.Y.H. and R.W. optimized the synthesis procedure and synthesized the single crystals. S.Y.H. and E.J.T. performed the SEM/EDX and analyzed the data. S.T. performed the STM and STS experiments. A.Z. collected and analyzed the TEM data. S.J.B. performed DFT calculations. S.Y.H. and E.J.T. performed the low-field magnetometry. S.Y.H., E.J.T., and E-S.C. performed the high-field magnetometry. S.Y.H. prepared the single-crystal transport devices, and E.J.T. performed the transport measurements and analyzed the data. A.K. collected and analyzed the ARPES data. T.-D.L. performed the XPS experiments. S.Y.H. and E.J.T. exfoliated few-layer flakes and performed the atomic force microscopy and contrast analysis. S.Y.H. and E.J.T. performed heat capacity measurements and analyzed the data. S.Y.H. performed and analyzed the PXRD data. The manuscript was prepared with input from all coauthors.

Notes

The authors declare no competing financial interest.

■ ACKNOWLEDGMENTS

We would like to thank Daniel Chica and Amymarie Bartholomew for their help in analyzing SCXRD data and Mike Ziebel for useful discussions on magnetic data. We would also like to acknowledge the use of Python-based data acquisition software developed by Maëlle Kapfer for all transport measurements. Synthesis and structural/compositional characterization of layered metallic antiferromagnets were supported by the National Science Foundation (NSF) through the Columbia University Materials Research Science and Engineering Center (MRSEC) on Precision-Assembled Quantum Materials DMR-2011738. Magnetotransport measurements were supported as part of Programmable Quantum Materials, an Energy Frontier Research Center funded by the U.S. Department of Energy (DOE), Office of Science, Basic Energy Sciences (BES), under award DE-SC0019443. Magnetic characterization was supported by the Air Force Office of Scientific Research award FA9550-22-1-0389. Imaging experiments were supported by the NSF CAREER award DMR-1751949. S.J.B. acknowledges support from the NSF Award DGE-2036197. The authors acknowledge the use of facilities and instrumentation supported by the NSF through Columbia University, Columbia Nano Initiative, and the Materials Research Science and Engineering Center DMR-2011738. The National High Magnetic Field Laboratory is supported by the NSF through NSF/DMR-1644779 and the State of Florida. The research at Brookhaven National Laboratory was supported by the US Department of Energy, Office of Basic Energy Sciences, Contract No. DESC0012704.

■ ABBREVIATIONS:

vdW, van der Waals; 2D, Two-dimensional; DFT, Density functional theory; ARPES, Angle-resolved photoemission spectroscopy; LIP, Long-in-plane; SIP, Short-in-plane; OOP, Out-of-plane; PDMS, Polydimethylsiloxane; SCXRD, Single crystal X-ray diffraction; SEM, Scanning electron microscopy; EDX, Energy dispersive X-ray spectroscopy; STM, Scanning tunneling microscopy; STS, Scanning tunneling spectroscopy; FFT, Fast Fourier transform; DOS, Density of states; TEM, Transmission electron microscopy; SAED, Selected-area electron diffraction; ZFC, Zero-field-cooled; FC, Field-cooled; MRR, Magnetoresistance ratio; nMRR, Negative magnetoresistance ratio; UHV, Ultrahigh vacuum; FS, Fermi surface; EDC, Energy distribution curve

■ REFERENCES

(1) Ahn, E. C. 2D materials for spintronic devices. *npj 2D Materials and Applications* **2020**, *4* (1), 17.
(2) Arora, A. Magneto-optics of layered two-dimensional semiconductors and heterostructures: Progress and prospects. *J. Appl. Phys.* **2021**, *129* (12), No. 120902.
(3) Hendriks, F.; Guimarães, M. H. D. Enhancing magneto-optic effects in two-dimensional magnets by thin-film interference. *AIP Advances* **2021**, *11* (3), No. 035132.
(4) Zhang, Y.; Xu, H.; Feng, J.; Wu, H.; Yu, G.; Han, X. Magnetic two-dimensional van der Waals materials for spintronic devices*. *Chinese Physics B* **2021**, *30* (11), No. 118504.
(5) Lan, T.; Ding, B.; Liu, B. Magneto-optic effect of two-dimensional materials and related applications. *Nano Select* **2020**, *1* (3), 298−310.
(6) Chen, Z.; Wang, B.; Xing, D. Y.; Wang, J. A spin injector. *Appl. Phys. Lett.* **2004**, *85* (13), 2553−2555.
(7) Ningrum, V. P.; Liu, B.; Wang, W.; Yin, Y.; Cao, Y.; Zha, C.; Xie, H.; Jiang, X.; Sun, Y.; Qin, S.; et al. Recent Advances in Two-Dimensional Magnets: Physics and Devices towards Spintronic Applications. *Research* **2020**, *2020*, 1−19.
(8) Wang, Q. H.; Bedoya-Pinto, A.; Blei, M.; Dismukes, A. H.; Hamo, A.; Jenkins, S.; Koperski, M.; Liu, Y.; Sun, Q.-C.; Telford, E. J.; et al. The Magnetic Genome of Two-Dimensional van der Waals Materials. *ACS Nano* **2022**, *16* (5), 6960−7079.
(9) Shin, I.; Cho, W. J.; An, E.-S.; Park, S.; Jeong, H.-W.; Jang, S.; Baek, W. J.; Park, S. Y.; Yang, D.-H.; Seo, J. H.; et al. Spin−Orbit Torque Switching in an All-Van der Waals Heterostructure. *Adv. Mater.* **2022**, *34* (8), No. 2101730.
(10) Martin, F.; Lee, K.; Schmitt, M.; Liedtke, A.; Shahee, A.; Simensen, H. T.; Scholz, T.; Saunderson, T. G.; Go, D.; Gradhand, M.; et al. Strong bulk spin−orbit torques quantified in the van der Waals ferromagnet Fe3GeTe2. *Materials Research Letters* **2023**, *11* (1), 84−89.
(11) Jungwirth, T.; Marti, X.; Wadley, P.; Wunderlich, J. Antiferromagnetic spintronics. *Nat. Nanotechnol.* **2016**, *11* (3), 231−241.
(12) Rezende, S. M.; Azevedo, A.; Rodríguez-Suárez, R. L. Introduction to antiferromagnetic magnons. *J. Appl. Phys.* **2019**, *126* (15), No. 151101.
(13) Yan, H.; Feng, Z.; Qin, P.; Zhou, X.; Guo, H.; Wang, X.; Chen, H.; Zhang, X.; Wu, H.; Jiang, C.; et al. Electric-Field-Controlled Antiferromagnetic Spintronic Devices. *Adv. Mater.* **2020**, *32* (12), No. 1905603.
(14) Ueda, K. Electrical Resistivity of Antiferromagnetic Metals. *J. Phys. Soc. Jpn.* **1977**, *43* (5), 1497−1508.
(15) Zhang, X.-X.; Jiang, S.; Lee, J.; Lee, C.; Mak, K. F.; Shan, J. Spin Dynamics Slowdown near the Antiferromagnetic Critical Point in Atomically Thin FePS3. *Nano Lett.* **2021**, *21* (12), 5045−5052.
(16) Bai, H.; Zhou, X.; Zhou, Y.; Chen, X.; You, Y.; Pan, F.; Song, C. Functional antiferromagnets for potential applications on high-density storage and high frequency. *J. Appl. Phys.* **2020**, *128* (21), No. 210901.
(17) Rahman, S.; Torres, J. F.; Khan, A. R.; Lu, Y. Recent Developments in van der Waals Antiferromagnetic 2D Materials: Synthesis, Characterization, and Device Implementation. *ACS Nano* **2021**, *15* (11), 17175−17213.
(18) Mak, K. F.; Shan, J.; Ralph, D. C. Probing and controlling magnetic states in 2D layered magnetic materials. *Nature Reviews Physics* **2019**, *1* (11), 646−661.
(19) Neuhausen, J.; Potthoff, E.; Tremel, W.; Ensling, J.; Gütlich, P.; Kremer, R. K. TaFe1.14Te3, A New Low-Dimensional Ternary

Tantalum Telluride. *Zeitschrift für Naturforschung B* **1993**, *48* (6), 797−811.
(20) Pérez Vicente, C.; Womes, M.; Jumas, J. C.; Sánchez, L.; Tirado, J. L. Distribution of Cations and Vacancies in TaFe1.25Te3 Studied by Mössbauer Spectroscopy. *J. Phys. Chem. B* **1998**, *102* (44), 8712−8718.
(21) Badding, M. E.; Li, J.; DiSalvo, F. J.; Zhou, W.; Edwards, P. P. Characterization of TaFe1.25Te3, a new layered telluride with an unusual metal network structure. *J. Solid State Chem.* **1992**, *100* (2), 313−324.
(22) Opačić, M.; Lazarević, N.; Tanasković, D.; Radonjić, M. M.; Milosavljević, A.; Ma, Y.; Petrovic, C.; Popović, Z. V. Small influence of magnetic ordering on lattice dynamics in ${\mathrm{TaFe}}_{1.25}{\mathrm{Te}}_{3}$. *Phys. Rev. B* **2017**, *96* (17), No. 174303.
(23) Ke, X.; Qian, B.; Cao, H.; Hu, J.; Wang, G. C.; Mao, Z. Q. Magnetic structure of quasi-one-dimensional antiferromagnetic TaFe${}_{1+y}$Te${}_{3}$. *Phys. Rev. B* **2012**, *85* (21), No. 214404.
(24) Liu, R. H.; Zhang, M.; Cheng, P.; Yan, Y. J.; Xiang, Z. J.; Ying, J. J.; Wang, X. F.; Wang, A. F.; Ye, G. J.; Luo, X. G.; et al. Spin-density-wave transition of Fe1 zigzag chains and metamagnetic transition of Fe2 in TaFe${}_{1+y}$Te${}_{3}$. *Phys. Rev. B* **2011**, *84* (18), No. 184432.
(25) Liu, Y.; Bao, J. J.; Xu, C. Q.; Jiao, W. H.; Zhang, H.; Xu, L. C.; Zhu, Z.; Yang, H. Y.; Zhou, Y.; Ren, Z.; et al. Coupling between antiferromagnetic and spin-glass orders in the quasi-one-dimensional iron telluride ${\mathrm{TaFe}}_{1+x}{\mathrm{Te}}_{3}$ ($x = 0.25$). *Phys. Rev. B* **2021**, *104* (10), No. 104418.
(26) Roy Chowdhury, R.; DuttaGupta, S.; Patra, C.; Kataria, A.; Fukami, S.; Singh, R. P. Anisotropic magnetotransport in the layered antiferromagnet ${\mathrm{TaFe}}_{1.25}{\mathrm{Te}}_{3}$. *Physical Review Materials* **2022**, *6* (8), No. 084408.
(27) Xu, M.; Wang, L.-M.; Peng, R.; Ge, Q.-Q.; Chen, F.; Ye, Z.-R.; Zhang, Y.; Chen, S.-D.; Xia, M.; Liu, R.-H.; et al. Electronic Structure Reconstruction across the Antiferromagnetic Transition in TaFe 1.23 Te 3 Spin Ladder. *Chin. Phys. Lett.* **2015**, *32* (2), No. 027401.
(28) Aruga, H.; Ito, A.; Wakabayashi, H.; Goto, T. Field-Dependent Phenomena in Reentrant-Spin-Glass: Fe(x)Mn(1-x)TiO(3) with x = 0.60, 0.65, and 0.75. *J. Phys. Soc. Jpn.* **1988**, *57* (8), 2636−2639.
(29) Ito, A.; Morimoto, S.; Aruga, H. Studies on Spin-Glass Freezing and Antiferromagnetic Long-Range Order in an Ising Spin-Glass System Fe(x)Mn(1-x)TiO(3). *Hyperfine Interact.* **1990**, *54*, 567−570.
(30) Katori, H. A.; Ito, A. Magnetic Property and Phase Diagram of a Frustrated System with Competing Exchange Interactions, Fe(x)-Mn(1-x)TiO(3). *J. Phys. Soc. Jpn.* **1993**, *62* (12), 4488−4502.
(31) Yoshizawa, H.; Mitsuda, S.; Aruga, H.; Ito, A. Reentrant Spin-Glass Transition and a Mixed Phase in an Ising System Fe(x)Mn(1-x)TiO(3). *J. Phys. Soc. Jpn.* **1989**, *58* (4), 1416−1426.
(32) Yamashita, T.; Hayes, P. Analysis of XPS spectra of Fe2+ and Fe3+ ions in oxide materials. *Appl. Surf. Sci.* **2008**, *254* (8), 2441−2449.
(33) Girit, Ç. Ö.; Zettl, A. Soldering to a single atomic layer. *Appl. Phys. Lett.* **2007**, *91* (19), No. 193512.
(34) Kerelsky, A.; McGilly, L. J.; Kennes, D. M.; Xian, L.; Yankowitz, M.; Chen, S.; Watanabe, K.; Taniguchi, T.; Hone, J.; Dean, C.; et al. Maximized electron interactions at the magic angle in twisted bilayer graphene. *Nature* **2019**, *572* (7767), 95−100.
(35) Pugh, E. M.; Rostoker, N. Hall Effect in Ferromagnetic Metals. *Rev. Mod. Phys.* **1953**, *25* (1), 151−157.
(36) Zhang, Y.; Chen, F.; He, C.; Yang, L. X.; Xie, B. P.; Xie, Y. L.; Chen, X. H.; Fang, M.; Arita, M.; Shimada, K.; et al. Strong correlations and spin-density-wave phase induced by a massive spectral weight redistribution in $\ensuremath{\alpha}{\text{-Fe}}_{1.06}\text{Te}$. *Phys. Rev. B* **2010**, *82* (16), No. 165113.
(37) Xu, X.; Li, Y. W.; Duan, S. R.; Zhang, S. L.; Chen, Y. J.; Kang, L.; Liang, A. J.; Chen, C.; Xia, W.; Xu, Y.; et al. Signature for non-Stoner ferromagnetism in the van der Waals ferromagnet $\mathrm{F}{\mathrm{e}}_{3}\mathrm{GeT}{\mathrm{e}}_{2}$. *Phys. Rev. B* **2020**, *101* (20), No. 201104.
(38) Schmitt, S.; Grewe, N.; Jabben, T. Itinerant and local-moment magnetism in strongly correlated electron systems. *Phys. Rev. B* **2012**, *85* (2), No. 024404.
(39) Liu, Z. K.; He, R. H.; Lu, D. H.; Yi, M.; Chen, Y. L.; Hashimoto, M.; Moore, R. G.; Mo, S. K.; Nowadnick, E. A.; Hu, J.; et al. Measurement of Coherent Polarons in the Strongly Coupled Antiferromagnetically Ordered Iron-Chalcogenide ${\mathrm{Fe}}_{1.02}\mathrm{Te}$ using Angle-Resolved Photoemission Spectroscopy. *Phys. Rev. Lett.* **2013**, *110* (3), No. 037003.
(40) Chen, Q. Y.; Luo, X. B.; Xie, D. H.; Li, M. L.; Ji, X. Y.; Zhou, R.; Huang, Y. B.; Zhang, W.; Feng, W.; Zhang, Y.; et al. Orbital-Selective Kondo Entanglement and Antiferromagnetic Order in ${\mathrm{USb}}_{2}$. *Phys. Rev. Lett.* **2019**, *123* (10), No. 106402.
(41) Zhang, Y.; He, C.; Ye, Z. R.; Jiang, J.; Chen, F.; Xu, M.; Ge, Q. Q.; Xie, B. P.; Wei, J.; Aeschlimann, M.; et al. Symmetry breaking via orbital-dependent reconstruction of electronic structure in detwinned NaFeAs. *Phys. Rev. B* **2012**, *85* (8), No. 085121.
(42) Yang, L. X.; Zhang, Y.; Ou, H. W.; Zhao, J. F.; Shen, D. W.; Zhou, B.; Wei, J.; Chen, F.; Xu, M.; He, C.; et al. Electronic Structure and Unusual Exchange Splitting in the Spin-Density-Wave State of the ${\mathrm{BaFe}}_{2}{\mathrm{As}}_{2}$ Parent Compound of Iron-Based Superconductors. *Phys. Rev. Lett.* **2009**, *102* (10), No. 107002.
(43) Kundu, A. K.; Barman, S.; Menon, K. S. R. Role of Surface Termination in the Metal−Insulator Transition of V2O3(0001) Ultrathin Films. *ACS Appl. Mater. Interfaces* **2021**, *13* (17), 20779−20787.
(44) Meinders, M. B. J.; Eskes, H.; Sawatzky, G. A. Spectral-weight transfer: Breakdown of low-energy-scale sum rules in correlated systems. *Phys. Rev. B* **1993**, *48* (6), 3916−3926.

https://doi.org/10.1021/acs.nanolett.3c03112
Nano Lett. 2023, 23, 10449−10457